Efficient Adiabatic Demagnetization Refrigeration to below 50 mK with Ultrahigh-Vacuum-Compatible Ytterbium Diphosphates $A\mathrm{YbP_2O_7}$ (A=Na, K)

U. Arjun,[1,2,*] K.M. Ranjith,[3] A. Jesche,[2,†] F. Hirschberger,[2] D.D. Sarma,[1] and P. Gegenwart[2,‡]

[1] *Solid State and Structural Chemistry Unit, Indian Institute of Science, Bengaluru 560012, India*

[2] *Experimental Physics VI, Center for Electronic Correlations and Magnetism, Institute of Physics, University of Augsburg, Augsburg 86135, Germany*

[3] *Laboratoire National des Champs Magnétiques Intenses-EMFL, CNRS, Université Grenoble Alpes, Grenoble 38042, France*

(Received 24 March 2023; revised 26 May 2023; accepted 12 June 2023; published 10 July 2023)

Attaining millikelvin (mK) temperatures is often a prerequisite for the study of quantum phenomena and the operation of quantum devices. Adiabatic demagnetization refrigeration (ADR) is an effective, easy, and sustainable alternative to evaporation or dilution cooling with the rare and superexpensive ^{3}He. Paramagnetic salts, traditionally used for mK ADR, suffer from chemical instability related to water of crystallization. We report synthesis, characterization, as well as low-temperature magnetization and specific heat measurements of two alternative UHV-compatible candidate materials $\mathrm{NaYbP_2O_7}$ and $\mathrm{KYbP_2O_7}$. Utilizing the physical property measurement system at 2 K, the ADR of sintered pellets with Ag powder admixture starting at 5 T yields base temperatures (warm-up times) of 45 mK (55 min) and 37 mK (35 min) for $\mathrm{NaYbP_2O_7}$ and $\mathrm{KYbP_2O_7}$, respectively, slightly advantageous to $\mathrm{KBaYb(BO_3)_2}$ (45 mK and 40 min) studied under similar conditions.

DOI: 10.1103/PhysRevApplied.20.014013

I. INTRODUCTION

Quantum effects are most evident at low temperatures where the thermal fluctuations are suppressed. Quantum effects such as Bose-Einstein condensation [1], superconductivity [2], quantum Hall effect [3], quantum spin liquid [4], quantum spin ice [5], etc., have been experimentally discovered only at temperatures close to absolute zero. The global scarcity of helium [6,7] and the increasing need for refrigeration for various technological applications enhanced the relevance of helium-free magnetic refrigeration techniques. The isotope ^{3}He, used in these refrigeration techniques, is extremely scarce in availability and thus extraordinarily expensive due to its increased demand in the defence sector for the production of neutron detectors to combat nuclear terrorism [8–10].

The significant temperature changes in some magnetic materials due to the magneto-caloric effect (MCE) while exposed to an external field [11] make them useful for attaining low temperatures through adiabatic demagnetization refrigeration (ADR) [12–14]. Currently millikelvin (mK) ADR is intensively used in satellites and other space technologies [15–19] and has already been shown to be potentially practical for quantum computers [20]. More generally, MCE-based magnetic refrigeration significantly reduces environmental impact and offers energy savings of nearly 30% compared to conventional techniques that use refrigerant gases [21].

For ADR applications, replacing a ^{3}He-^{4}He dilution refrigerator, materials with a significant entropy change ΔS in the temperature range between 10 mK and 4 K are required. They should also exhibit a strong MCE within the lowest possible applied magnetic field. In the multistage process for attaining subkelvin temperatures, the material is first precooled to a temperature of about 2 K in a magnetic field of typically a few teslas (e.g., using a pumped ^{4}He bath or a pulse-tube cooler). Subsequently, the thermal contact with the bath is cut by pumping out the He gas or opening a heat switch, and the cooling substance is demagnetized. In this adiabatic process, the very low entropy of the cooling substance due to precooling in the magnetic field requires that the temperature of the cooling substance is significantly lowered, ideally below 50 mK.

A major disadvantage of ADR compared to ^{3}He-^{4}He dilution refrigeration has been its incapability of continuous cooling, which is being addressed by the recent developments in continuous ADR [16,22]. Commercial continuous refrigerators based on ADR are now available

*arjunu@iisc.ac.in
†anton.jesche@physik.uni-augsburg.de
‡philipp.gegenwart@physik.uni-augsburg.de

[23], suggesting that ADR has the potential to become a major refrigeration technology.

Even several decades after the first realization of magnetic refrigeration down to the mK range, hydrated paramagnetic salts with very low ordering temperatures are commonly used as cooling substances in ADR refrigerators. In the paramagnetic salts, the spins are very much diluted and are almost noninteracting, resulting in a low volumetric cooling power and low thermal conductivity. By contrast, systems with a higher number of magnetic ions per unit volume may exhibit stronger exchange interactions, resulting in magnetic order. The magnetic ordering typically prevents the system from cooling down adiabatically to lower temperatures.

Even in almost-ideal paramagnets, there may be a very weak magnetic interaction J through which the neighboring spins can interact weakly even at $H = 0$, resulting in a small internal field. This can lead to a tiny Zeeman splitting (Δ_0) and magnetic ordering at a temperature of the same energy scale. Magnetic ordering suddenly drops the entropy to zero and limits the final ADR temperature to $T_f \sim \Delta_0 \sim J$, since the entropy difference between $H = 0$ and a finite H is a crucial parameter for ADR [24]. A perfect paramagnet with zero interaction and maximum entropy at $H = 0$ close to 0 K is an ideal refrigerant. But in real paramagnetic materials, the presence of a finite weak interaction is inevitable.

Recently the disordered quantum magnets came into focus. Since entropy accumulates near quantum critical points and/or due to magnetic frustration, alternative strategies for obtaining efficient mK ADR were explored [24–35]. In frustrated quantum magnets, the enhanced quantum fluctuations suppress the long-range ordering, despite the strong spin interactions, giving rise to a shift of entropy towards low temperatures, that is crucial for obtaining lower ADR end temperatures [24]. For the efficiency of the cooling substance, the available entropy change per volume is an essential parameter [36]. The size of the spins and their density contribute to the volumetric entropy density, which should be as high as possible.

Traditional mK ADR substances such as $CrK(SO_4)_2 \cdot 12H_2O$ (CPA) [37] incorporate water of crystallization for separation of magnetic ions. Hence, the magnetic interactions are sufficiently small, resulting in very low magnetic ordering temperatures, like 30 mK for CPA. However, these salts have high water vapor pressure and, therefore, cannot be evacuated. This requires vacuum-tight encapsulation of the active material in a protective container. In order to ensure sufficient thermal coupling of very poorly thermally conductive salts, it is also necessary to grow them as single crystals within a very fine wire network [36]. This complex production of encapsulated cooling units leads to high costs. Furthermore, they must not be heated due to the lack of chemical stability. This means that they cannot be thoroughly baked above 100 °C for UHV applications.

Oxide quantum magnets, on the other hand, are stable upon heating and evacuation. Recently, it was discovered that potassium-barium-ytterbium borate $KBaYb(BO_3)_2$ can be used as an inert, easy-to-produce and inexpensive cooling substance for UHV-compatible adiabatic demagnetization cooling [24]. Magnetic order in $KBaYb(BO_3)_2$ is hindered by both geometrical frustration on the triangular lattice as well as the statistical mixing of K^+ and Ba^{2+}, resulting in uneven electric fields acting on the Yb^{3+} ions, eventually causing a wide distribution of magnetic couplings. Isostructural $KBaGd(BO_3)_2$ shows magnetic order below $T_N = 263$ mK in zero field, reaches a minimal ADR temperature of 122 mK and warm-up time of 8 h in the physical property measurement system (PPMS) setup [38]. Dipolar and magnetic exchange couplings are of similar magnitude in this system [38,39]. Taking into consideration that dipolar and exchange interactions are proportional to the square of the magnetic moment and using the measured saturation moments for $KBaYb(BO_3)_2$ and $KBaGd(BO_3)_2$, suggests a magnetic order at 9 mK in the former [38].

In this work, we report mK magnetization, specific heat, and ADR measurements on the geometrically frustrated quantum magnets $NaYbP_2O_7$ and $KYbP_2O_7$. Similar to $KBaYb(BO_3)_2$ [24], the two materials are chemically stable and UHV-compatible. A direct comparison of the ADR performance with $KBaYb(BO_3)_2$ under similar conditions indicates for $NaYbP_2O_7$ a similar ADR end temperature but 30% longer hold time and for $KYbP_2O_7$ a 20% lower ADR end temperature at the cost of a 12.5% shorter hold time. Thus, the two diphosphates are superior candidates for UHV-compatible mK ADR.

II. METHODS

Synthesis: polycrystalline samples of $AYbP_2O_7$ (A = Na, K) are synthesized by the conventional solid-state reaction technique by annealing the stoichiometric mixture of Na_2CO_3/K_2CO_3 (99.99%), Yb_2O_3 (99.99%), and $NH_4H_2PO_4$ (99.99%) in an alumina boat at 650 °C for $NaYbP_2O_7$ and 600 °C for $KYbP_2O_7$ for a duration of 48 h with one intermediate grinding and pelletization. The synthesis procedures for the $KBaYb(BO_3)_2$ pellet used for the comparison of ADR performances are described in Ref. [24].

Powder x-ray diffraction: phase purities of the samples are confirmed by powder x-ray diffraction (XRD, PANalytical powder diffractometer with CuK_α radiation, $\lambda_{ave} = 1.54182$ Å) at room temperature. Rietveld refinement of the observed XRD patterns is performed using the `FullProf` package [40] (see Fig. 3), taking the initial parameters from Ref. [41,42].

dc magnetization: dc magnetization (M) is measured as a function of the temperature (T) down to 0.4 K and the applied magnetic field (H) up to 7 T in a MPMS-3 Quantum Design superconducting quantum interference device (SQUID) magnetometer with ^{3}He option.

Specific heat: specific heat $C_p(T)$ is measured using the heat-capacity option of a PPMS manufactured by Quantum Design. For the low-temperature (0.4 K $\leq T \leq$ 2.2 K) C_p measurements the ^{3}He option is used.

For strong thermal coupling, the specific heat measurements are performed on pellets made from sodium and potassium diphosphates (grain size 10–50 μm) mixed with fine silver powder (1 μm) in a mass ratio of 1 : 1. In order to extract the specific heat of the sample, we subtracted the Ag contribution from the measured data. In a magnetic insulator, the specific heat C_p contains significant contributions from the phonon excitations ($C_{\rm ph}$) and the magnetic lattice (C_m). At high temperatures, $C_p(T)$ is entirely dominated by $C_{\rm ph}$, while at low temperatures, it is dominated by C_m. In order to estimate the phonon part of the specific heat, the zero-field data are fitted by a polynomial function between 10 and 20 K (where no magnetic contribution is present), see Fig. S1 within the Supplemental Material [43]. Similar procedures have been used previously and have shown to be efficient for estimating $C_{\rm ph}$ in cases where heat-capacity data of nonmagnetic analog compounds are not available [44–47]. The fit is extrapolated down to low temperatures, and the magnetic specific heat C_m is obtained by subtracting the obtained $C_{\rm ph}$ values from the experimental C_p data. Magnetic entropy S_m is estimated by integrating $C_m(T)/T$ from 0.4 K to high temperatures as $S_m(T) = \int_{0.4\ K}^{T} \frac{C_m(T')}{T'} dT'$.

Adiabatic demagnetization refrigeration (ADR): using an ADR material in a commercial PPMS in order to achieve temperatures below 1.8 K without using ^{3}He presents an immediate practical application. For the cooling experiment, we use a 3.5 g cylindrical pellet of 6 mm thickness and 15 mm diameter containing equal weights of $AYbP_2O_7$ (grain diameter 10–50 μm) and silver powder (grain diameter 1 μm). Silver powder is used to improve the thermal conductivity within the pellet as $AYbP_2O_7$ is insulating in nature. Also, we sinter the pressed pellet at 600 °C to further improve the thermal conductivity.

We perform the ADR experiments in the PPMS with a similar setup as described in Refs. [24,38]. A sample stage is constructed in which the pellet is mounted on a plastic straw. The sample is thermally isolated from the heat bath. An RuO_2 resistor is glued as a thermometer on the pellet and is connected using thin resistive manganin wires to minimize the heat flow. The resistor is measured with a current of 1 nA utilizing a Lake-Shore 372 AC Bridge and reached a value of 31.65 kOhm for $KYbP_2O_7$ at the lowest temperature. A metallic cap is used as a shield to minimize the effect of surrounding thermal radiation. The sample is cooled to $T = 2$ K in a field of 5 T and subsequently the high-vacuum mode (pressure $< 10^{-4}$ mbar) is employed in order to achieve thermal decoupling. Then the magnetic field of 5 T is swept to zero at a rate of 0.15 T min^{-1}. At zero field the pellet reaches the lowest temperature and then slowly back up to 2 K by the slow heat flow from the bath. The imperfect adiabaticity mainly arises from the finite amount of exchange gas. Of course the vacuum would be improved, if the high-vacuum mode is already switched on at higher temperatures, but then a long hold time to reach the starting temperature 2 K would be necessary. We also perform ADR experiments with a $KBaYb(BO_3)_2$ pellet from Ref. [24] utilizing the same thermometer and procedure as in the case of $AYbP_2O_7$. This allows for a direct comparison of the ADR performances of the two diphosphates with that of the previously reported borate.

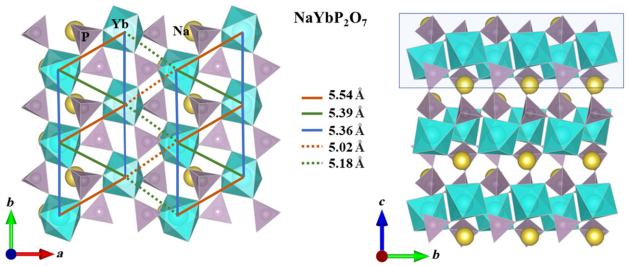

FIG. 1. Crystal structure of $NaYbP_2O_7$ in the a-b plane and along the c direction. The YbO_6 octahedra are linked via PO_4 tetrahedra and span a distorted triangular grid (left panel). One such triangular layer is highlighted by a rectangular box in the right panel. Different Yb-Yb distances are color coded.

III. RESULTS

A. Structure

Both $NaYbP_2O_7$ and $KYbP_2O_7$ crystallize in a monoclinic lattice with the space group $P21/c$ (No. 14) but form different structure types. The point symmetry of the Yb site is 1, thus the Yb^{3+} total angular momentum $J = 7/2$ splits into four Kramers doublets. The crystal structure of $NaYbP_2O_7$ consists of distorted YbO_6 octahedra, which are corner-shared with PO_4 tetrahedra, forming a magnetic Yb triangular layer in the crystallographic a-b plane. These triangular planes are well separated by two nonmagnetic PO_4 units and Na ions along the crystallographic c direction (see Fig. 1). In $KYbP_2O_7$, on the other hand, the YbO_6 octahedra are connected by PO_4 tetrahedra forming uniform chains running along the c axis and are connected by alternating chains in the a-c plane. It forms a three-dimensional distorted hyperhoneycomblike network (see Fig. 2).

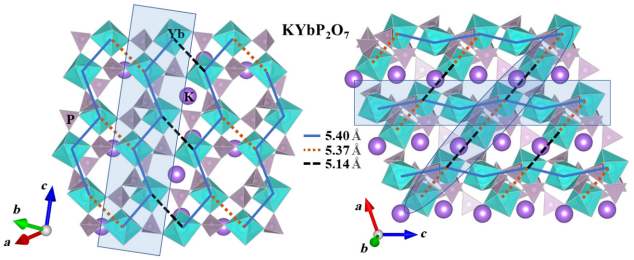

FIG. 2. Crystal structure of $KYbP_2O_7$. The YbO_6 octahedra are linked via PO_4 tetrahedra forming uniform chains running along the c axis (highlighted by a rectangular box), which are interconnected by alternating chains running in the a-c plane (highlighted by an ellipse in the right panel). This forms a three-dimensional distorted hyperhoneycomblike network. Different Yb-Yb distances are color coded.

B. Powder x-ray diffraction

Figure 3 shows the powder XRD pattern of $NaYbP_2O_7$ and $KYbP_2O_7$ at room temperature, along with the Rietveld refinement. For $NaYbP_2O_7$, the refinement uses the monoclinic space group $P2_1/c$ (No. 14) [settings $P2_1/n$ (unique axis b)], taking the initial parameters from Ref. [42]. The goodness of fit is $\chi^2 = 4.72$. The obtained lattice parameters are $a = 9.0215(1)$ Å, $b = 5.3599(1)$ Å, $c = 12.7816(1)$ Å, $\beta = 103.1655(1)^\circ$, and $V_{\text{cell}} \simeq 601.81(1)$ Å^3. These values are in close agreement with reported values [42]. For $KYbP_2O_7$, the refinement is performed using the monoclinic space group $P2_1/c$ (No. 14) [settings $P2_1/c$ (unique axis b)], taking the initial parameters from Ref. [41]. The goodness of fit is $\chi^2 = 8.78$. The obtained lattice parameters are $a = 7.5500(1)$ Å, $b = 10.8306(1)$ Å, $c = 8.5492(1)$ Å, $\beta = 106.7200(1)^\circ$, and $V_{\text{cell}} \simeq 669.52(1)$ Å^3. These values are in close agreement with the reported values [41]. The unit cell volume of $NaYbP_2O_7$ is small compared to $KYbP_2O_7$ because the ionic radius of Na^+ (1.18 Å) is smaller than that of K^+ (1.51 Å) [48].

C. Magnetization

The temperature-dependent magnetic susceptibility $\chi(T) = M/H$ data of $NaYbP_2O_7$ and $KYbP_2O_7$ are measured at applied fields $H = 0.1$ T and 1 T. No evidence of any long-range magnetic order is observed down to 0.4 K. At high temperatures (above 150 K), $1/\chi(T)$ can be well fitted with the modified Curie-Weiss (CW) expression (see Fig. 4)

$$\chi(T) = \chi_0 + \frac{C}{T - \theta_{\text{CW}}}, \tag{1}$$

where χ_0 is the temperature-independent contribution consisting of the diamagnetic susceptibility of core electron shells (χ_{core}) and the van Vleck paramagnetic susceptibility (χ_{VV}) of the open shells of the Yb^{3+} ions. The second term

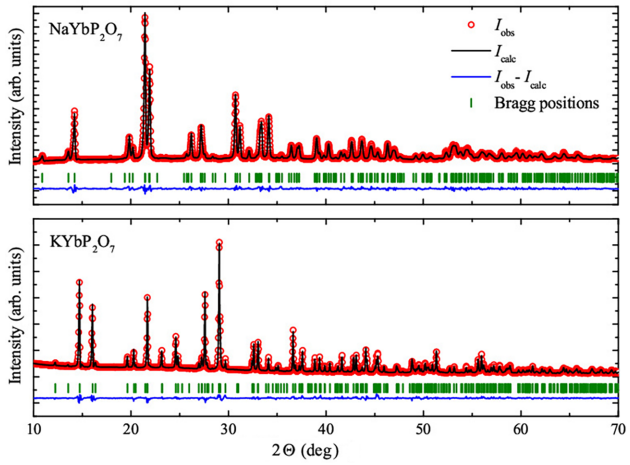

FIG. 3. Powder x-ray diffraction pattern (open red circles) for $NaYbP_2O_7$ (upper panel) and $KYbP_2O_7$ (lower panel) at room temperature. The solid line represents the Rietveld refinement, with the vertical bars showing the expected Bragg peak positions and the lower solid blue line representing the difference between observed and calculated intensities.

in Eq. (1) is the CW law with the CW temperature θ_{CW} and Curie constant $C = N_A\mu_{\text{eff}}^2/3k_B$. Here, N_A is Avogadro's number, $\mu_{\text{eff}} = g\sqrt{J(J+1)}\mu_B$ is the effective magnetic moment, g is the Landé g factor, μ_B is the Bohr magneton, and J is the effective spin.

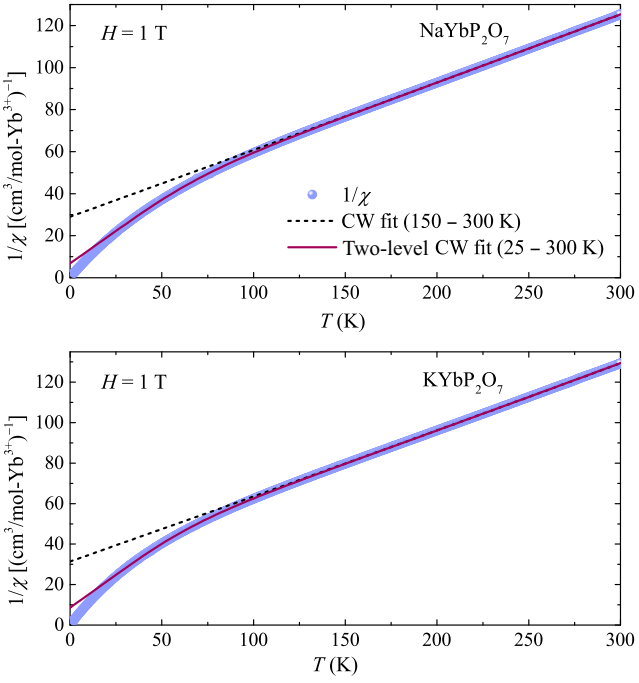

FIG. 4. Inverse magnetic susceptibility ($1/\chi$) data measured at 1 T as a function of temperature (T) for $NaYbP_2O_7$ (upper panel) and $KYbP_2O_7$ (lower panel). The dashed and solid lines represent the fits by Eqs. (1) and (2), respectively.

The fitting yields the parameters $\chi_0^{\rm HT} \simeq -1.73 \times 10^{-4}$ cm^3/mol, $C_{\rm HT} \simeq 3.20$ cm^{3}K/mol, and $\theta_{\rm CW}^{\rm HT} \simeq -92$ K for $NaYbP_2O_7$ and $\chi_0^{\rm HT} \simeq -2.48 \times 10^{-4}$cm^3/mol, $C_{\rm HT} \simeq 3.18$ cm^{3}K/mol, and $\theta_{\rm CW}^{\rm HT} \simeq -99$ K for $KYbP_2O_7$. Note, however, that these CW temperatures arise from the curvature below 100 K due to the crystal electric field (CEF) splitting and thus cannot be used to estimate magnetic couplings. The resulting effective moment $\mu_{\rm eff}^{\rm HT}$ is calculated to be $5.06\mu_B$ and $5.05\mu_B$ for $NaYbP_2O_7$ and $KYbP_2O_7$, respectively. These values of $\mu_{\rm eff}^{\rm HT}$ are in reasonable agreement with the expected value of $4.54\mu_B$ for the Yb^{3+} ($J = 7/2, g = 8/7$) ion in the $4f^{13}$ configuration.

A clear change in slope is observed in $1/\chi(T)$ data below 150 K, arising from thermal depopulation of excited CEF levels. Similar behavior is observed in several other Yb^{3+}-based spin systems. Typically, the combination of the spin-orbit coupling and the CEF leads to a Kramers doublet ground state for the Yb^{3+} ion, and the low-temperature properties can be described by an $S_{\rm eff} = 1/2$ ground state [49–54]. Our analysis of the entropy (below) indeed confirms a Kramers doublet ground state below 10 K.

Following Ref. [55] effective two-level CEF fits

$$1/\chi(T) = 8(T - \theta_{\rm CW}) \left(\frac{\mu_{\rm eff,1}^2 + \mu_{\rm eff,2}^2 \times e^{(-\Delta/T)}}{1 + e^{(-\Delta/T)}} \right)^{-1} \quad (2)$$

with splitting $\Delta = 231$ K for $NaYbP_2O_7$ and 220 K for $KYbP_2O_7$ can successfully describe the change in slope of the inverse susceptibility below 150 K, cf. the red lines in Fig. 4. The obtained values for $\mu_{\rm eff,1,2}$ and $\theta_{\rm CW}$ are $3.60\mu_B$, $5.89\mu_B$, and -11 K, respectively for $NaYbP_2O_7$, as well as $3.51\mu_B$, $5.83\mu_B$, and -13 K, respectively, for $KYbP_2O_7$. The values of $\mu_{\rm eff,1}$ and $\theta_{\rm CW}$ do not represent the lowest Kramers doublet, as evident by the deviation of the fit from the data below 40 K. A fit with four CEF levels and associated effective moments suffers from too many adjustable parameters. Therefore, we determine the properties related to the Kramers doublet ground state from magnetic measurements below 2 K.

The magnetization isotherms $M(H)$ of $KYbP_2O_7$ [see Fig. 5(a)] and $NaYbP_2O_7$ [see Fig. 5(b)] measured up to 7 T at $T = 0.4$ K show saturation around 1.5 T. The saturation values $M_{\rm sat}$ are estimated by fitting the high-field regions above 5 T with straight lines reflecting $\chi_0 H$ and extrapolating the lines back to zero field. This yields $\chi_0 \simeq 5.51 \times 10^{-3}$ cm^3/mol and $M_{\rm sat} \simeq 1.55\mu_B$ for $NaYbP_2O_7$ and $\chi_0 \simeq 4.11 \times 10^{-3}$ cm^3/mol and $M_{\rm sat} \simeq 1.47\mu_B$ for $KYbP_2O_7$. Using $\mu_{\rm sat} = g_{\rm eff} S_{\rm eff} \mu_B$ gives $g_{\rm eff}$ values of $\simeq 3.10$ for $NaYbP_2O_7$ and $\simeq 2.94$ for $KYbP_2O_7$. After subtracting χ_0, the $\chi(T)$ data below 2 K are fitted by the CW law $\chi(T) = C/(T - \theta_{\rm CW})$. The fitting yields $\theta_{\rm CW}^{\rm LT} \simeq (51 \pm 4)$ mK and $\mu_{\rm eff}^{\rm LT} \simeq 2.68\mu_B$ for $NaYbP_2O_7$ and $\theta_{\rm CW}^{\rm LT} \simeq (18 \pm 4)$ mK and $\mu_{\rm eff}^{\rm LT} \simeq 2.53\mu_B$ for $KYbP_2O_7$. The obtained effective moments are in good agreement with $\mu_{\rm eff} = g_{\rm eff}\sqrt{S_{\rm eff}(S_{\rm eff}+1)}\mu_B$ for a pseudo spin-1/2 ground state with $g_{\rm eff}$ values of 3.10 for $NaYbP_2O_7$ and 2.92 for $KYbP_2O_7$, consistent with those estimated from $M_{\rm sat}$.

Very small values of $\theta_{\rm CW}^{\rm LT}$ at low-T suggest the lack of significant exchange interactions between Yb^{3+} magnetic moments. According to mean field theory, $\theta_{\rm CW}$ is the sum of all possible exchange interactions [56]. Since there are many possible interaction pathways in the structure, as shown by Figs. 1 and 2, it is also possible that the

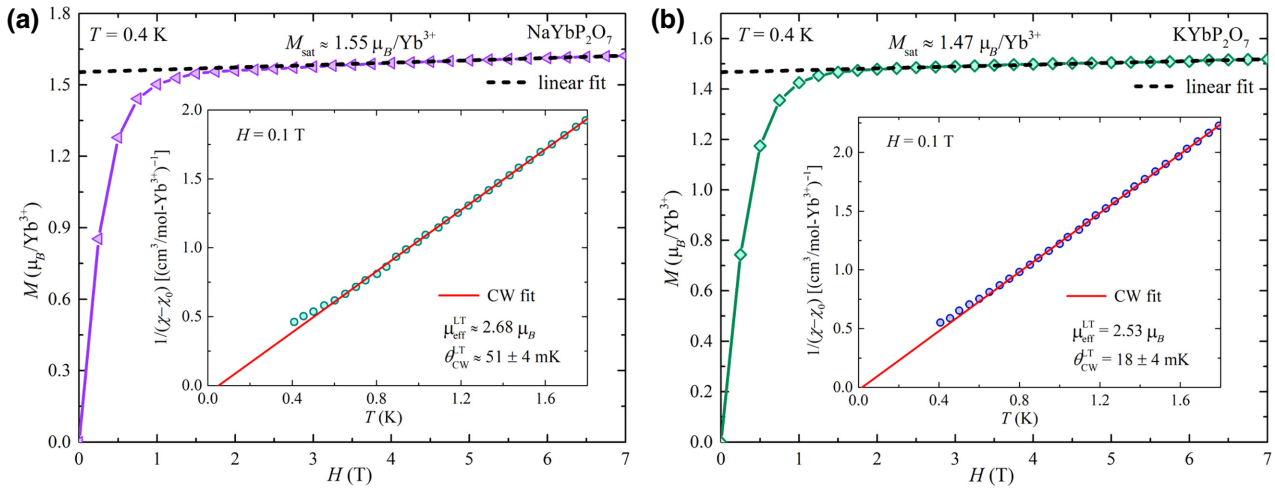

FIG. 5. Isothermal magnetization $M(H)$ measured at 0.4 K for $NaYbP_2O_7$ (a) and $KYbP_2O_7$ (b). Dashed lines represent linear contributions (see text). The insets show the low-temperature inverse magnetic susceptibility after subtracting χ_0 along with the CW fit for $NaYbP_2O_7$ [inset of (a)] and $KYbP_2O_7$ [inset of (b)].

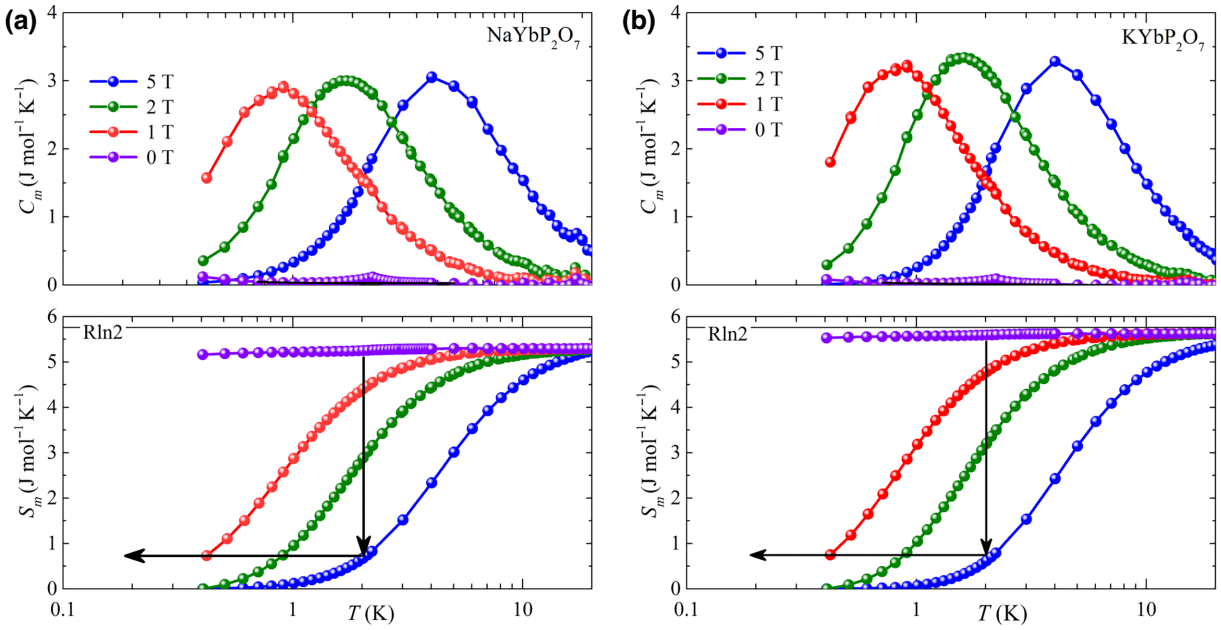

FIG. 6. Low-temperature magnetic specific heat (C_m) of $NaYbP_2O_7$ [upper panel of (a)] and $KYbP_2O_7$ [upper panel of (b)] at several external magnetic fields. Phonon contribution is subtracted from the raw data using a polynomial fit. Magnetic entropy (S_m) of $NaYbP_2O_7$ [lower panel of (a)] and $KYbP_2O_7$ [lower panel of (b)] calculated by integrating C_m/T. For fields below 2 T the entropy is vertically shifted to match the other curves at 20 K. Two arrows show the ADR process.

competing ferromagnetic and antiferromagnetic exchange interactions cancel each other, resulting in very small values of $\theta_{\rm CW}^{\rm LT}$.

D. Specific heat

The specific heat analyses of $NaYbP_2O_7$ and $KYbP_2O_7$ at different applied fields are shown in various panels of Fig. 6, suggesting their ADR potentials. The specific heat data of $NaYbP_2O_7$ and $KYbP_2O_7$ show no signatures of magnetic long-range ordering down to 0.4 K. In zero field, the specific heat shows an increase towards lower temperatures, suggesting the entropy accumulation associated with the Kramers doublet of Yb^{3+}. This doublet is split by the magnetic field into $j_z = +1/2$ and $j_z = -1/2$ levels, causing a Schottky anomaly that shifts toward higher temperatures with increasing field.

For $NaYbP_2O_7$ and $KYbP_2O_7$, the resulting magnetic entropy (S_m) saturates about 5.3 J/mol K and 5.6 J/mol K, respectively (see Fig. 6). The values agree quite well with the expected theoretical value $S_m = R\ln(2J+1)$ of 5.76 J/mol K for the Kramers doublet with $J_{\rm eff} = 1/2$. At 0 and 1 T, the entire entropy of $R\ln 2$ associated with the lowest Kramers doublet of Yb^{3+} could not be recovered as we did not measure below 0.4 K. Higher fields shift the entropy toward higher temperatures, so that at 2 T, almost complete entropy of $R\ln 2$ can be recovered above 0.4 K. The entropy data at 0 and 1 T, are vertically shifted to match values at higher fields (2 and 5 T). At 5 T, only approximately 10% of $R\ln 2$ remains at $T = 2$ K. Therefore, by adiabatic demagnetization starting from 2 K and 5 T, very low temperatures can be attained as indicated by arrows in Fig. 6.

In the zero-field specific heat data of $NaYbP_2O_7$ and $KYbP_2O_7$, a tiny anomaly at 2.23 K is found, arising from a Yb_2O_3 impurity contribution [57]. Integrating the entropy related to this impurity peak yields a negligible fraction of 0.6% of $R\ln 2$ related to the impurity contribution for both compounds (see Fig. S2 within the Supplemental Material [43]).

E. Adiabatic demagnetization refrigeration

The comparison of the cooling performances of $NaYbP_2O_7$ (red) and $KYbP_2O_7$ (green) with $KBaYb(BO_3)_2$ (yellow) in the commercial PPMS are shown in Fig. 7. The sample temperatures are plotted on the left y axis, while the external magnetic field is plotted on the right y axis. During demagnetization, the lowest temperature attained by $KYbP_2O_7$ is 37 mK while the lowest temperatures attained by $NaYbP_2O_7$ and $KBaYb(BO_3)_2$ are both 45 mK. A spike in the sample temperature around 70 mK is observed, possibly due to flux pinning of the superconducting magnet.

The time required for $NaYbP_2O_7$ to relax back from the lowest temperature to 2 K is 55 min, whereas the warming time for $KYbP_2O_7$ is shorter, i.e., about 35 min. The warming time of $NaYbP_2O_7$ is much longer than that of $KBaYb(BO_3)_2$ (40 min). Note that the hold times at low temperatures could be significantly enhanced by using a

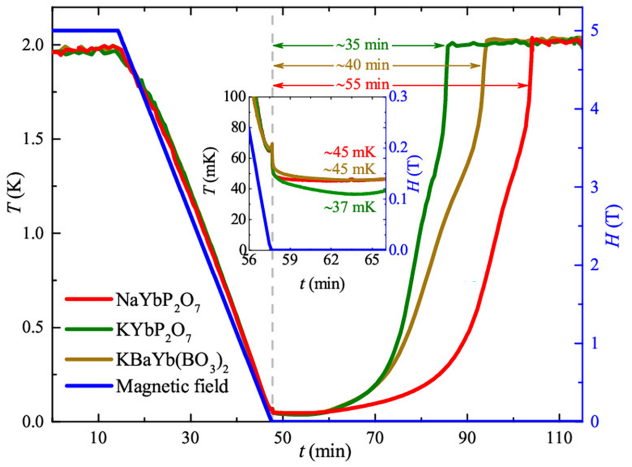

FIG. 7. ADR performance comparison of $NaYbP_2O_7$ (red), $KYbP_2O_7$ (green), and $KBaYb(BO_3)_2$ (brown) in the commercial physical property measurement system (PPMS). The sample is slowly cooled to $T = 2$ K at $H = 5$ T through the weak thermal link to the PPMS puck kept at 2 K and the 'high-vacuum mode' of the PPMS was employed in order to achieve thermal decoupling. Subsequently, magnetic field is swept from 5 T to zero at a rate of 0.15 T min^{-1} and the temperature change with time t is recorded. The blue curve shows the respective magnetic field.

thermal shield and precooling ADR station for all connected wires. But already in this simple setup, the warm-up times are sufficient to use the setup, for instance, to perform temperature-dependent electrical resistance measurements on small samples. Of note, the obtained base temperatures are much lower as for the commercially available ADR option for the PPMS, which uses CPA and reaches a minimum temperature of 100 mK [58].

IV. DISCUSSION

The low-temperature properties of both $NaYbP_2O_7$ and $KYbP_2O_7$ can be well described by an effective spin-1/2 ground state expected for Yb^{3+}-based quantum magnets. Very small CW temperatures obtained from the analysis of the susceptibility data at low temperatures indicate the absence of significant interactions between the Yb moments, which is advantageous to achieve low final temperatures in ADR measurements.

The compounds $NaYbP_2O_7$ and $KYbP_2O_7$ have proven to be very efficient for ADR applications because they do not contain water molecules and are stable to heating and evacuation. It can be seen from Fig. 6 that almost all of the entropy ($R \ln 2$) of the lowest Kramers doublet can be used for cooling, even at a moderate magnetic field of 5 T, similar to the conventionally used paramagnetic salts [14]. The crucial parameters determining the efficiency of various known ADR materials are compared in Table I. The full entropy of the ground state is described as $S_{GS} = R \ln(2J + 1)$, and the entropy density S_{GS}/vol. is calculated by dividing S_{GS} by the unit-cell volume. A large value of S_{GS} is always beneficial because the magnetic entropy changes (ΔS_m) of magnetic refrigerants act as the driving force of ADR. However, it is worth noting that for practical purposes, the relevant quantity is not the molar entropy but rather the volumetric entropy density S_{GS} of the material.

TABLE I. Comparison of relevant parameters of different mK ADR materials: T_m is the magnetic ordering temperature, S_{GS} is the entropy of the ground-state multiplet, and R is the universal gas constant. The abbreviations are MAS = $Mn(NH_4)_2(SO_4)_2 \cdot 6H_2O$ (manganese ammonium sulfate), FAA = $NH_4Fe(SO_4) \cdot 12H_2O$ (ferric ammonium alum), CPA = $KCr(SO_4) \cdot 12H_2O$ (chromium potassium alum), CMN = $Mg_3Ce_2(NO_3)_{12} \cdot 24H_2O$ (cerium magnesium nitrate).

Material	ADR materials		S_{GS}	S_{GS}/vol. [mJ/(K cm^3)]
	T_m (mK)	mag. ion/vol. (nm^{-3})		
MAS [59]	170	2.8	$R \ln 6$	70
FAA [59]	30	2.1	$R \ln 6$	53
CPA [37]	10	2.2	$R \ln 4$	42
CMN [60]	2	1.7	$R \ln 2$	16
$YbPt_2Sn_{12}$ [28]	250	12.9	$R \ln 2$	124
$Yb_3Ga_5O_{12}$ [29]	54	13.2	$R \ln 2$	124
$KBaYb(BO_3)_2$ [24]	< 22	6.7	$R \ln 2$	64
$NaYbP_2O_7$	< 45	6.6	$R \ln 2$	64
$KYbP_2O_7$	< 37	6.0	$R \ln 2$	57

As can be seen from Table I, materials with high entropy density such as $YbPt_2Sn$ or $Yb_3Ga_5O_{12}$ exhibit magnetic orderings at 250 and 54 mK, respectively, which limit their lowest attainable temperatures as the entropies drop to zero below the ordering temperatures. The high-temperature paramagnetic salts such as MAS and FAA, which have a larger magnetic entropy $R \ln 6$ are also affected by their much higher magnetic ordering temperatures. On the other hand, low transition temperature materials such as CPA and CMN have low magnetic moment density and hence low entropy density. A high entropy density usually contradicts a low magnetic ordering temperature.

In this context, it has been reported that the disordered quantum magnet $KBaYb(BO_3)_2$ exhibits these two mutually exclusive criteria, such as a high volumetric entropy density (64 mJ/(K cm^3)) combined with a very low ordering at approximately 9 mK [38], allowing ADR to be well below 20 mK [24]. In this compound, the magnetic frustration and the structural randomness help to suppress the magnetic order. Because of its suitable properties, $KBaYb(BO_3)_2$ has been proven to be an excellent anhydrous ADR refrigerant. By demagnetizing $H = 5$ T at 2 K in PPMS, a minimal temperature of 40 mK was attained with pellets mixed of $KBaYb(BO_3)_2$ powder with Ag powder [24]. Utilizing a better adiabatic setup in the dilution

refrigerator with feedback control of the bath temperature following the sample temperature, $KBaYb(BO_3)_2$ cooled upon demagnetization starting at 5 T from 2 K to well below 20 mK [24].

$NaYbP_2O_7$ and $KYbP_2O_7$ have also high magnetic ion densities (6.6 and 6 nm^{-3}) and volumetric entropy densities [64 and 57 $mJ/(K\,cm^3)$]. These values are comparable to those of $KBaYb(BO_3)_2$ but are much higher than those of the paramagnetic ADR salts for the mK application. The comparative study of the ADR performance of $AYbP_2O_7$ and $KBaYb(BO_3)_2$ pellets under exactly similar conditions reveal a significantly lower minimal temperature of 37 mK for $KYbP_2O_7$, whereas $NaYbP_2O_7$ reaches the same minimum temperature of 45 mK as $KBaYb(BO_3)_2$ but with the advantage of a much longer warm-up time. Comparison with our previous work on $KBaYb(BO_3)_2$ [24] suggests that $KYbP_2O_7$ and $NaYbP_2O_7$ can also be cooled by demagnetization to significantly lower temperatures of at least 20 mK in better adiabatic conditions (as realized previously for the former utilizing a ^{3}He- ^{4}He dilution refrigerator).

Compared to commercially used conventional mK ADR coolants based on paramagnetic salts, $AYbP_2O_7$ and $KBaYb(BO_3)_2$ are anhydrous compounds and hence stable at high vacuum and high temperatures up to at least 600 °C. Therefore, an encapsulated installation is not required, making them user friendly and suitable for UHV applications. Finally, excellent thermal contact can be achieved in easily prepared pellets by mixing powder samples with silver powder in 1:1 ratio. Overall, it has been shown that all three cooling substances are very well suited for UHV-compatible ADR down to 50 mK.

V. CONCLUSION

In summary, we perform a comprehensive study on the low-temperature properties of two Yb-based quantum magnets $NaYbP_2O_7$ and $KYbP_2O_7$ and compare their mK ADR performance with $KBaYb(BO_3)_2$. The low-temperature properties are well described by very weakly interacting $J_{\rm eff} = 1/2$ Kramers doublets of the Yb^{3+} ions. ADR experiments in the PPMS under comparable conditions for all three compounds confirm that all the three are highly suitable to achieve temperatures below 50 mK. With respect to $KBaYb(BO_3)_2$, $KYbP_2O_7$ yields a 20% lower temperature (but 12.5% shorter hold time), while for $NaYbP_2O_7$ a similar end temperature is combined with 30% longer hold time compared to $KBaYb(BO_3)_2$. Both diphosphates are thus excellent new UHV-compatible mK ADR materials.

ACKNOWLEDGMENTS

We thank Marvin Klinger and Yoshi Tokiwa for useful discussions. U.A. would like to acknowledge DST, India, for financial support bearing sanction (DST/INSPIRE/04/2019/001664). Work supported by the German Science Foundation through projects 107745057 (TRR80) and 514162746 (GE 1640/11-1). D.D.S. thanks SERB, DST, and CSIR, Government of India, for financial support. We note that a German patent for the usage of ABP_2O_7 (A=alkaline metal, B=rare earth) for UHV compatible ADR to very low temperatures has been filed by the University of Augsburg (file reference DE 10 2023 106 074.0, March 10, 2023).

[1] V. Zapf, M. Jaime, and C. Batista, Bose-Einstein condensation in quantum magnets, Rev. Mod. Phys. **86**, 563 (2014).
[2] H. K. Onnes, The Superconductivity of Mercury, Comm. Phys. Lab. Univ., Leiden **122**, 122 (1911).
[3] M. O. Goerbig, Electronic properties of graphene in a strong magnetic field, Rev. Mod. Phys. **83**, 1193 (2011).
[4] Y. Zhou, K. Kanoda, and T.-K. Ng, Quantum spin liquid states, Rev. Mod. Phys. **89**, 025003 (2017).
[5] S. T. Bramwell and M. J. Harris, The history of spin ice, J. Phys. Condens. Matter **32**, 374010 (2020).
[6] L. M. Kelley, Challenging "helium scarcity", Chemical Engineering **110**, 8 (2003).
[7] A. H. Olafsdottir and H. U. Sverdrup, Assessing the Past and Future Sustainability of Global Helium Resources, Extr, Supply Use, Using Integr. Assessment Model WORLD7, Biophys. Econ. Sustainability **5**, 1 (2020).
[8] R. T. Kouzes and J. H. Ely, *Status summary of ^{3}He and neutron detection alternatives for homeland security* (2010).
[9] D. A. Shea and D. Morgan, The helium-3 shortage: Supply, demand, and options for congress (Library of Congress Washington DC, 2011).
[10] A. Cho, Helium-3 shortage could put freeze on low-temperature research, Science **326**, 778 (2009).
[11] P. Weiss and A. Piccard, Le phénomène magnétocalorique, J. Phys. Theor. Appl. **7**, 103 (1917).
[12] P. Debye, Einige Bemerkungen zur Magnetisierung bei tiefer Temperatur, Ann. der Phys. **386**, 1154 (1926).
[13] W. Giauque and D. MacDougall, Attainment of temperatures below 1° absolute by demagnetization of $Gd_2(SO_4)_3 \cdot 8H_2O$, Phys. Rev. **43**, 768 (1933).
[14] F. Pobell, *Matter and Methods at Low Temperatures* (Springer, Berlin, Heidelberg, 2007), 3rd ed.
[15] P. J. Shirron, Applications of the magnetocaloric effect in single-stage, multi-stage and continuous adiabatic demagnetization refrigerators, Cryogenics **62**, 130 (2014).
[16] P. Shirron, E. Canavan, M. DiPirro, J. Francis, M. Jackson, J. Tuttle, T. King, and M. Grabowski, Development of a cryogen-free continuous ADR for the constellation-X mission, Cryogenics **44**, 581 (2004).
[17] P. J. Shirron, Cooling capabilities of adiabatic demagnetization refrigerators, J. Low Temp. Phys. **148**, 915 (2007).
[18] N. Luchier, J. Duval, L. Duband, P. Camus, G. Donnier-Valentin, and M. Linder, 50 mK cooling solution with an ADR precooled by a sorption cooler, Cryogenics **50**, 591 (2010).

[19] C. Hagmann and P. Richards, Adiabatic demagnetization refrigerators for small laboratory experiments and space astronomy, Cryogenics **35**, 303 (1995).

[20] A. E. Jahromi, P. J. Shirron, and M. J. DiPirro, in *2019 Cryogenic Engineering Conference and International Cryogenic Materials Conference (CEC/ICMC)*, GSFC-E-DAA-TN70637 (2019).

[21] A. Alahmer, M. Al-Amayreh, A. O. Mostafa, M. Al-Dabbas, and H. Rezk, Magnetic refrigeration design technologies: State of the art and general perspectives, Energies **14**, 15 (2021).

[22] J. Bartlett, G. Hardy, I. Hepburn, C. Brockley-Blatt, P. Coker, E. Crofts, B. Winter, S. Milward, R. Stafford-Allen, and M. Brownhill, *et al.*, Improved performance of an engineering model cryogen free double adiabatic demagnetization refrigerator, Cryogenics **50**, 582 (2010).

[23] Kiutra, see, e.g., Cooling technology: Solid-state cryogen-free cooling, https://kiutra.com/technology/.

[24] Y. Tokiwa, S. Bachus, K. Kavita, A. Jesche, A. A. Tsirlin, and P. Gegenwart, Frustrated magnet for adiabatic demagnetization cooling to milli-kelvin temperatures, Commun. Mater. **2**, 1 (2021).

[25] X.-Y. Liu, Y. Gao, H. Li, W. Jin, J. Xiang, H. Jin, Z. Chen, W. Li, and G. Su, Quantum spin liquid candidate as superior refrigerant in cascade demagnetization cooling, Commun. Phys. **5**, 1 (2022).

[26] M. Kleinhans, K. Eibensteiner, J. Leiner, J. Spallek, A. Regnat, and C. Pfleiderer, Magnetocaloric properties of $(RE)_3Ga_5O_{12}$ (RE = Tb, Gd, Nd, Dy), Phys. Rev. Appl. **19**, 014038 (2023).

[27] B. Wolf, Y. Tsui, D. Jaiswal-Nagar, U. Tutsch, A. Honecker, K. Remović-Langer, G. Hofmann, A. Prokofiev, W. Assmus, G. Donath, and M. Lang, Magnetocaloric effect and magnetic cooling near a field-induced quantum-critical point, Proc. Natl. Acad. Sci. **108**, 6862 (2011).

[28] D. Jang, T. Gruner, A. Steppke, K. Mitsumoto, C. Geibel, and M. Brando, Large magnetocaloric effect and adiabatic demagnetization refrigeration with $YbPt_2Sn$, Nat. Commun. **6**, 1 (2015).

[29] D. A. P. Brasiliano, J.-M. Duval, C. Marin, E. Bichaud, J.-P. Brison, M. Zhitomirsky, and N. Luchier, YbGG material for adiabatic demagnetization in the 100 mK–3 K range, Cryogenics **105**, 103002 (2020).

[30] Y. Tokiwa, B. Piening, H. S. Jeevan, S. L. Bud'ko, P. C. Canfield, and P. Gegenwart, Super-heavy electron material as metallic refrigerant for adiabatic demagnetization cooling, Sci. Adv. **2**, e1600835 (2016).

[31] M. Evangelisti, O. Roubeau, E. Palacios, A. Camón, T. N. Hooper, E. K. Brechin, and J. J. Alonso, Cryogenic magnetocaloric effect in a ferromagnetic molecular dimer, Angew. Chem. Int. Ed. **50**, 6606 (2011).

[32] A. Baniodeh, N. Magnani, Y. Lan, G. Buth, C. E. Anson, J. Richter, M. Affronte, J. Schnack, and A. K. Powell, High spin cycles: topping the spin record for a single molecule verging on quantum criticality, npj Quantum Mater. **3**, 1 (2018).

[33] M. Zhitomirsky, Enhanced magnetocaloric effect in frustrated magnets, Phys. Rev. B **67**, 104421 (2003).

[34] B. Wolf, U. Tutsch, S. Dörschug, C. Krellner, F. Ritter, W. Assmus, and M. Lang, Magnetic cooling close to a quantum phase transition–the case of $Er_2Ti_2O_7$, J. Appl. Phys. **120**, 142112 (2016).

[35] Y. Hu and A. Du, Magnetization behavior and magnetic entropy change of frustrated Ising antiferromagnets on two- and three-dimensional lattices, J. Phys. Condens. Matter **20**, 125225 (2008).

[36] P. Wikus, E. Canavan, S. T. Heine, K. Matsumoto, and T. Numazawa, Magnetocaloric materials and the optimization of cooling power density, Cryogenics **62**, 150 (2014).

[37] J. Daniels and N. Kurti, The thermal and magnetic properties of chromium potassium alum below 0.1 K, Proc. R. Soc. A **221**, 243 (1954).

[38] A. Jesche, N. Winterhalter-Stocker, F. Hirschberger, A. Bellon, S. Bachus, Y. Tokiwa, A. A. Tsirlin, and P. Gegenwart, Adiabatic demagnetization cooling well below the magnetic ordering temperature in the triangular antiferromagnet $KBaGd(BO_3)_2$, Phys. Rev. B **107**, 104402 (2023).

[39] J. Xiang, C. Su, N. Xi, Z. Fu, Z. Chen, H. Jin, Z. Chen, Z.-J. Mo, Y. Qi, J. Shen, L. Zhang, W. Jin, W. Li, P. Sun, and G. Su, Dipolar spin liquid ending with quantum critical point in a Gd-based triangular magnet, ArXiv:2301.03571.

[40] J. Rodríguez-Carvajal, Recent advances in magnetic structure determination by neutron powder diffraction, Phys. B: Condens. Matter **192**, 55 (1993).

[41] K. Horchani-Naifer and M. Férid, Potassium ytterbium diphosphate, Acta Crystallogr. Sect. E: Struct. Rep. Online **63**, i33 (2007).

[42] M. Férid, K. Horchani-Naifer, and M. Trabelsi-Ayedi, Crystal structure of sodium ytterbium diphosphate $NaYbP_2O_7$, Z. Kristallogr. NCS **219**, 385 (2004).

[43] See Supplemental Material at http://link.aps.org/supplemental/10.1103/PhysRevApplied.20.014013 for additional information on the specific heat data analysis.

[44] S. Guchhait, U. Arjun, P. K. Anjana, M. Sahoo, A. Thirumurugan, A. Medhi, Y. Skourski, B. Koo, J. Sichelschmidt, B. Schmidt, M. Baenitz, and R. Nath, Case study of bilayered spin-1/2 square lattice compound $VO(HCOO)_2 \cdot (H_2O)$, Phys. Rev. Mater. **3**, 104409 (2019).

[45] R. Nath, M. Padmanabhan, S. Baby, A. Thirumurugan, D. Ehlers, M. Hemmida, H.-A. Krug von Nidda, and A. A. Tsirlin, Quasi-two-dimensional S=1/2 magnetism of $Cu[C_6H_2(COO)_4][C_2H_5NH_3]_2$, Phys. Rev. B **91**, 054409 (2015).

[46] T. Matsumoto, Y. Miyazaki, A. S. Albrecht, C. P. Landee, M. M. Turnbull, and M. Sorai, Heat capacities of the S = 1/2 two-dimensional Heisenberg antiferromagnet bis(2-amino-5-chloropyridinium) tetrabromocuprate(ii) $[(5CAP)_2CuBr_4]$ and its diamagnetic analogue $(5CAP)_2ZnBr_4]$, J. Phys. Chem. B **104**, 9993 (2000).

[47] T. Lancaster, S. J. Blundell, M. L. Brooks, P. J. Baker, F. L. Pratt, J. L. Manson, M. M. Conner, F. Xiao, C. P. Landee, F. A. Chaves, S. Soriano, M. A. Novak, T. P. Papageorgiou, A. D. Bianchi, T. Herrmannsdörfer, J. Wosnitza, and J. A. Schlueter, Magnetic order in the s=1/2 two-dimensional molecular antiferromagnet copper pyrazine perchlorate $Cu(Pz)_2(ClO_4)_2$, Phys. Rev. B **75**, 094421 (2007).

[48] R. D. Shannon, Revised effective ionic radii and systematic studies of interatomic distances in halides and chalcogenides, Acta Cryst. **A32**, 751 (1976).

[49] J. A. Paddison, M. Daum, Z. Dun, G. Ehlers, Y. Liu, M. B. Stone, H. Zhou, and M. Mourigal, *et al.*, and Continuous excitations of the triangular-lattice quantum spin liquid $YbMgGaO_4$, Nat. Phys. **13**, 117 (2017).

[50] M. M. Bordelon, E. Kenney, C. Liu, T. Hogan, L. Posthuma, M. Kavand, Y. Lyu, M. Sherwin, N. P. Butch, and C. Brown, *et al.*, Field-tunable quantum disordered ground state in the triangular-lattice antiferromagnet $NaYbO_2$, Nat. Phys. **15**, 1058 (2019).

[51] K. M. Ranjith, S. Luther, T. Reimann, B. Schmidt, P. Schlender, J. Sichelschmidt, H. Yasuoka, A. Strydom, Y. Skourski, and J. Wosnitza, *et al.*, Anisotropic field-induced ordering in the triangular-lattice quantum spin liquid $NaYbSe_2$, Phys. Rev. B **100**, 224417 (2019).

[52] M. Baenitz, P. Schlender, J. Sichelschmidt, Y. Onykiienko, Z. Zangeneh, K. Ranjith, R. Sarkar, L. Hozoi, H. Walker, and J.-C. Orain, *et al.*, $NaYbS_2$: A planar spin-1/2 triangular-lattice magnet and putative spin liquid, Phys. Rev. B **98**, 220409 (2018).

[53] B. Schmidt, J. Sichelschmidt, K. M. Ranjith, T. Doert, and M. Baenitz, Yb delafossites: Unique exchange frustration of $4f$ spin-$\frac{1}{2}$ moments on a perfect triangular lattice, Phys. Rev. B **103**, 214445 (2021).

[54] K. M. Ranjith, D. Dmytriieva, S. Khim, J. Sichelschmidt, S. Luther, D. Ehlers, H. Yasuoka, J. Wosnitza, A. A. Tsirlin, H. Kühne, and M. Baenitz, Field-induced instability of the quantum spin liquid ground state in the $J_{\text{eff}} = \frac{1}{2}$ triangular-lattice compound $NaYbO_2$, Phys. Rev. B **99**, 180401 (2019).

[55] S. Mugiraneza and A. M. Hallas, Tutorial: A beginner's guide to interpreting magnetic susceptibility data with the Curie-Weiss law, Commun. Phys. **5**, 95 (2022).

[56] C. Domb and A. R. Miedema, *Progress in Low Temperature Physics*, edited by C. J. Gorter, Vol. 4 (Elsevier, North-Holland, Amsterdam, 1964), p. 296.

[57] R. M. Moon, H. R. Child, W. C. Koehler, and L. J. Raubenheimer, Magnetic structure of Er_2O_3 and Yb_2O_3, J. Appl. Phys. **38**, 1383 (1967).

[58] Quantum Design PPMS Platform Measurement Options, https://www.qdusa.com/siteDocs/productBrochures/1084-500.pdf.

[59] O. E. Vilches and J. C. Wheatley, Measurements of the specific heats of three magnetic salts at low temperatures, Phys. Rev. **148**, 509 (1966).

[60] R. A. Fisher, E. W. Hornung, G. E. Brodale, and W. F. Giauque, Magnetothermodynamics of $Ce_2Mg_3(NO_3)_{12} \cdot 24H_2O$. II. The evaluation of absolute temperature and other thermodynamic properties of CMN to 0.6 mK, J. Chem. Phys. **58**, 5584 (1973).